



# 1 **WRF-Comfort: Simulating micro-scale variability of outdoor heat** 2 **stress at the city scale with a mesoscale model**

3 Alberto Martilli<sup>1</sup>, Negin Nazarian<sup>2,3</sup>, E. Scott Krayenhoff<sup>4</sup>, Jacob Lachapelle<sup>4</sup>, Jiachen Lu<sup>2,3</sup>, Esther  
4 Rivas<sup>1</sup>, Alejandro Rodriguez-Sanchez<sup>1</sup>, Beatriz Sanchez<sup>1</sup>, Jose Luis Santiago<sup>1</sup>

5 <sup>1</sup>Atmospheric Modelling Unit, Environmental Department, CIEMAT, Madrid, 28040, Spain

6 <sup>2</sup>School of Built Environment, University of New South Wales, Sydney, Australia

7 <sup>3</sup>ARC Centre of Excellence for Climate Extremes, Australia

8 <sup>4</sup>School of Environmental Sciences, University of Guelph, Guelph, Canada

9 *Correspondence to:* Alberto Martilli (alberto.martilli@ciemat.es)

10 **Abstract.** Urban overheating, and its ongoing exacerbation due to global warming and urban development, leads to  
11 increased exposure to urban heat and increased thermal discomfort and heat stress. To quantify thermal stress, specific  
12 indices have been proposed that depend on air temperature, mean radiant temperature (MRT), wind speed, and relative  
13 humidity. While temperature and humidity vary on scales of hundreds of meters, MRT and wind speed are strongly affected  
14 by individual buildings and trees, and vary at the meter scale. Therefore, most numerical thermal comfort studies apply  
15 micro-scale models to limited spatial domains (commonly representing urban neighborhoods with building blocks) with  
16 resolutions on the order of 1 m and a few hours of simulation. This prevents the analysis of the impact of city-scale  
17 adaptation/mitigation strategies on thermal stress and comfort. To solve this problem, we develop a methodology to estimate  
18 thermal stress indicators and their subgrid variability in mesoscale models - here applied to the multilayer urban canopy  
19 parametrization BEP-BEM within the WRF model. The new scheme (consisting of three main steps) can readily assess  
20 intra-neighborhood scale heat stress distributions across whole cities and for time scales of minutes to years. The first key  
21 component of the approach is the estimation of MRT in several locations within streets for different street orientations.  
22 Second, mean wind speed, and its subgrid variability, are parameterized as a function of the local urban morphology based  
23 on relations derived from a set of microscale LES and RANS simulations across a wide range of realistic and idealized urban  
24 morphologies. Lastly, we compute the distributions of two thermal stress indices for each grid square combining all the  
25 subgrid values of MRT, wind speed, air temperature, and absolute humidity. From these distributions, we quantify the high  
26 and low tails of the heat stress distribution in each grid square across the city, representing the thermal diversity experienced  
27 in street canyons. In this contribution, we present the core methodology as well as simulation results for Madrid (Spain),  
28 which illustrate strong differences between heat stress indices and common heat metrics like air or surface temperature, both  
29 across the city and over the diurnal cycle.

30



## 31 1 Introduction

32 The combination of urban development and climate change has increased heat exposure in cities in recent decades (Tuholske  
33 et al., 2021) and a continuation of these trends in the 21st century would be difficult to offset locally from an air temperature  
34 perspective (Broadbent et al., 2020; Krayenhoff et al., 2018; Zhao et al., 2021). Adaptation options that target contributions  
35 to heat exposure other than the air temperature, such as radiation (e.g., via shade) and wind (e.g. via improved street  
36 ventilation), should therefore be considered. Quantification of these contributions relative to air temperature requires the  
37 application of comprehensive thermo-physiological heat stress metrics such as the Universal Thermal Climate Index, UTCI  
38 (Jendritzky et al., 2012), the Physiological Equivalent Temperature, PET (Höppe, 1999), or the Standard Effective  
39 Temperature, SET (Gagge et al., 1986). Moreover, exposure to heat hazards is moderated by infrastructure-based and  
40 social/mobility-based adaptations to heat, and by buildings and associated cooling mechanisms. Here, the focus is the  
41 development of a tool to quantify the outdoor component of heat exposure in cities, accounting for all relevant  
42 meteorological variables.

43 Heat exposure in urban areas is affected by several meteorological variables that vary on different spatial and temporal scales  
44 (Nazarian et al., 2022). While temperature and humidity vary on spatial scales on the order of hundreds of meters, shortwave  
45 and longwave radiation and wind speed are strongly affected by individual buildings and vary at the scale of a few meters.  
46 For this reason, most numerical thermal comfort studies in urban areas apply micro-scale models with resolutions on the  
47 order of 1 m and spatial domains that are limited to an urban block or neighborhood (Nazarian et al., 2017; Zhang et al.,  
48 2022; Geletič et al., 2018). While these studies include substantial detail at the micro-scale, they are very expensive  
49 computationally and therefore can be applied only to a few neighborhoods and they neglect the interactions with larger scale  
50 meteorological phenomena (e.g., land/sea breezes, mountain/valley winds, urban breezes) that often play a relevant role in  
51 outdoor thermal comfort and its variation across cities. On the other hand, contemporary meso-scale numerical models can  
52 be applied to the whole urban area and surrounding regions, and therefore capture these larger-scale phenomena, but have  
53 spatial resolutions of several hundred meters at best. These models use a grid mesh that does not resolve buildings and is  
54 therefore too coarse to capture the fine-scale variation of radiation and wind flow of relevance to outdoor heat exposure and  
55 ultimately thermal comfort.

56 The objective of this work is to fill the aforementioned gap by developing a model that includes the most crucial capabilities  
57 of micro-scale assessments of thermal exposure within meso-scale models. This new model will quantify the spatial  
58 variability (i.e., statistical representation of the microscale distribution) for longwave and shortwave radiation as well as  
59 wind speed within each meso-scale grid square. Subsequently, it will capture the range of thermal exposure, as quantified by  
60 the UTCI and SET thermal stress metrics, within each urban grid square across a city at each time of day. The focus here is  
61 on the *range* of thermal exposure, such that we identify the cool and hot spots within the grid cell without having to resolve  
62 the entire spatial distribution. We argue that this represents the most crucial information for heat management and urban  
63 design interventions, as it identifies whether people can move and search for optimal thermal conditions. For example, if hot



64 spots are experiencing extreme heat stress but the cool spots are at slight heat stress, pedestrians have the opportunity, and  
65 autonomy, to seek shade and thermal respite (i.e., spatial autonomy as described in Nazarian et al. (2019)). Conversely, if the  
66 conditions in the cool spot are already in extreme heat stress, this can be used to inform urban design interventions or heat  
67 advisories to vulnerable populations to avoid being outside at that place and time. Overall, representing the range of heat  
68 exposure at the neighborhood scale while covering regional-scale phenomena is key to human-centric assessments of urban  
69 overheating (Nazarian et al., 2022).

70 The new model is embedded in the multi-layer urban canopy parameterization BEP-BEM (Martilli et al., 2002; Salamanca et  
71 al., 2010) which simulates the local-scale meteorological effects of the grid average urban morphology within the Weather  
72 Research and Forecasting (WRF) mesoscale model (Skamarock et al., 2019 version 4.3 has been used in this study). Here,  
73 BEP-BEM is extended to quantify the spatial variation of the mean radiant temperature and wind speed within the grid  
74 square at the pedestrian level. To our knowledge, three schemes in the published literature have attempted to capture thermal  
75 exposure in an urban canopy model. Pigliautile (2020) implemented a scheme to estimate human thermal exposure in the  
76 Princeton Single-Layer Urban Canopy Model. However, the scheme has not been run within a mesoscale model. Jin et al.  
77 (2022) calculate urban mean radiant temperature (MRT) in a mesoscale model, while Lemonsu (2015) and Leroyer et al.  
78 (2018) assess UTCI in mesoscale modeling applications within Paris and Toronto, respectively. Moreover, Giannaros et al  
79 (2018, 2023), made an offline coupling of WRF-BEP\_BEM with RayMan (Matzarakis et al. 2007). However, none of these  
80 approaches account for the within-grid spatial variation of wind speed, and their assessment of sub-grid spatial variation of  
81 radiation exposure (i.e., mean radiant temperature) is limited. Here, we further extend the BEP-BEM model embedded in the  
82 WRF meso-scale model to overcome these limitations and more fully assess spatial variation of thermal exposure within  
83 each urban grid square.

84 In section 2, the methodology is described in detail, with a focus on model development and implementation in WRF. In  
85 Section 3, we present an example of the type of outputs that can be produced. Conclusions are in section 4.

## 86 **2 Methodology**

87 The most complete thermal stress indices invariably depend on four meteorological variables: air temperature, mean radiant  
88 temperature (MRT), relative humidity, and wind speed. Among these, MRT and wind speed have the largest spatial  
89 variability in the urban canopy, and this variability is often captured with 3D micro-scale models of urban airflow and  
90 radiative heat transfer. At the meso-scale, however, it is not feasible to incorporate such models, motivating the simplified  
91 urban canopy parameterizations developed here. Below we detail how the BEP-BEM urban canopy model is modified to a)  
92 introduce a simplified model for MRT variation within a meso-scale grid cell (Sec. 2.1) and b) parameterize airflow  
93 variability (Sec. 2.2) in the urban canopy within a grid cell, and make a simple estimate of air temperature variability. These  
94 meteorological parameters are then used to estimate the sub-grid scale variation of thermal stress indices (Sec. 2.3), namely



95 SET and UTCI, as two of the most commonly used indices for outdoor environments (Potchter et al 2018). Lastly, we  
96 discuss how multi-scale temporal and spatial variabilities in thermal exposure can be effectively communicated using the  
97 outcomes of the updated WRF-BEP-BEM model.

## 98 2.1 A simplified model for MRT variability in the urban canopy

99 The mean radiant temperature is a measure of the total radiation flux absorbed by the human body, including both shortwave  
100 (from the sun, either directly or after reflection on the walls or road) and longwave (emitted from solid bodies like walls or  
101 road, or from the sky) radiation. Whether pedestrians are shaded or in the sunshine, as well as their distance from warm  
102 surfaces emitting radiation, is therefore very important. BEP-BEM applies a simple urban morphology: two street canyons of  
103 different orientations, each with the same street width and building height distribution on each side of the canyon (Martilli et  
104 al. 2002). To capture the within-grid spatial extremes of mean radiant temperature, we assess pedestrian locations at the  
105 center of the street for two canyon orientations considered in BEP-BEM and at positions located at a distance of 1.5 m from  
106 the building wall on each side of the street, representing the sidewalks. Thus, there are 6 positions (three for each street  
107 direction) in each urban grid square where we compute the mean radiant temperature (shown for the example of North-South  
108 and East-West streets in Fig. 1). For shortwave reflection and longwave emission and reflection, the standard BEP view  
109 factor and shading routines (Martilli et al. 2002) are used to estimate the amount of shortwave (direct and diffuse) and  
110 longwave radiation reaching a vertical segment 1.80 m tall and located in each of the six positions previously mentioned  
111 (Fig. 1). Reflection of shortwave radiation and emission and reflection of longwave radiation from both building walls and  
112 the street surface are accounted for via these view factors. The pedestrian is “transparent” from the perspective of the urban  
113 facets, meaning that its presence does not alter the shortwave and longwave radiation reaching the building walls and road.  
114 The mean radiant temperature is computed by weighting the radiation reaching each side of the vertical segment by 0.44, and  
115 the radiation reaching the downward- and upward-facing (at 1.80 m height) surfaces of the pedestrian by 0.06 each. This  
116 approach follows the six-directional weighting method (Thorsson et al. 2007) and aggregates the four lateral weightings of  
117 0.22 into two lateral weightings of 0.44 since BEP-BEM is a two-dimensional model (e. g. the streets are considered  
118 infinitely long). Namely,

$$119 \quad T_{MRT} = \sqrt[4]{\frac{\sum_{i=1,4} W_i (a_K K_i + a_L L_i)}{a_L \sigma}} \quad (1)$$

120 where, for an N-S oriented street,  $i=1,2$  are for the vertical sides of the pedestrian looking East, and West respectively, and  
121  $i=3,4$  are for the top and bottom. Therefore,  $W_{1,2}=0.44$ , while  $W_{3,4}=0.06$ ,  $a_K=0.7$ , and  $a_L=0.97$ ,  $K_{1,2}$  and  $L_{1,2}$  are the short and  
122 longwave radiation reaching the vertical segment, and  $K_{3,4}$  and  $L_{3,4}$  are short and longwave radiation reaching the top and  
123 bottom respectively, and  $\sigma$  is the Stefan-Boltzmann constant.

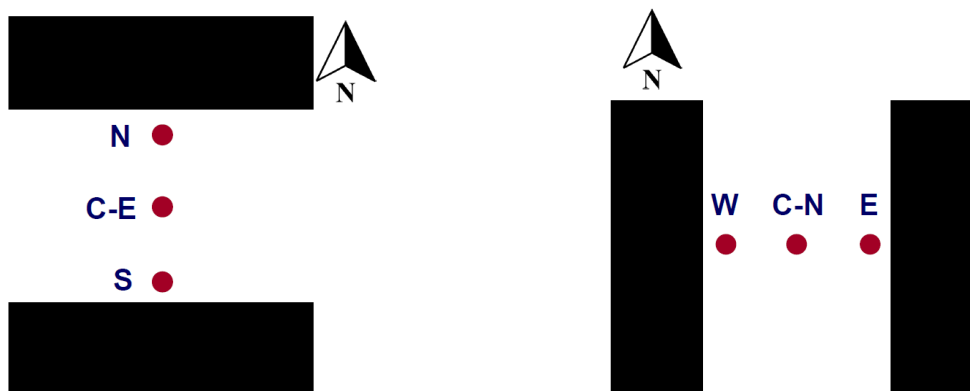
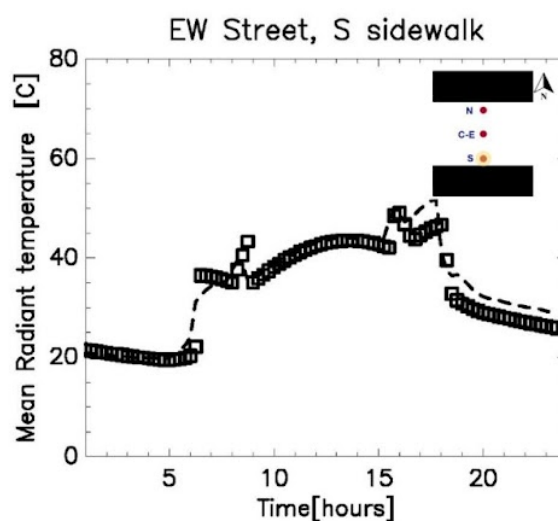
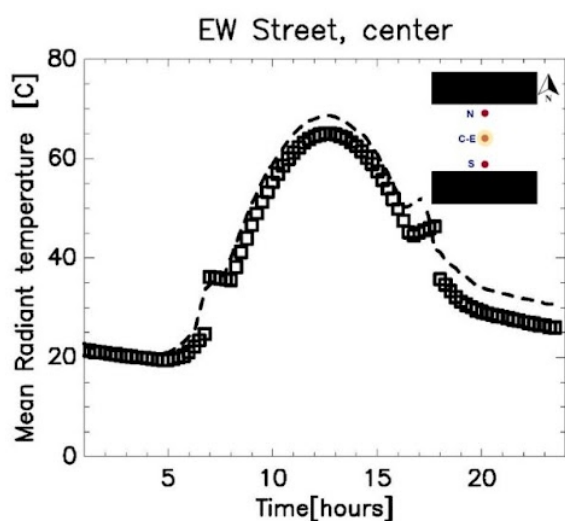
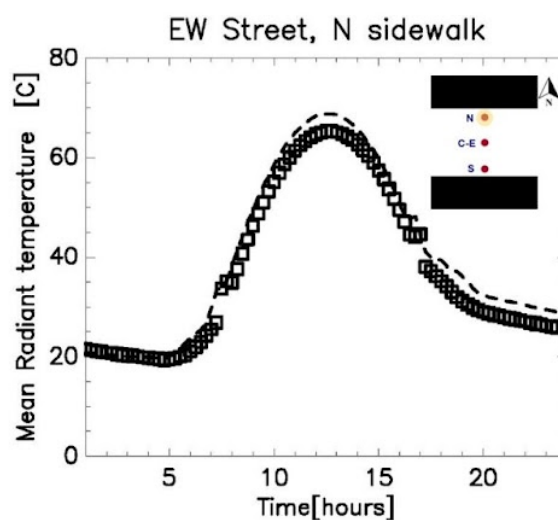
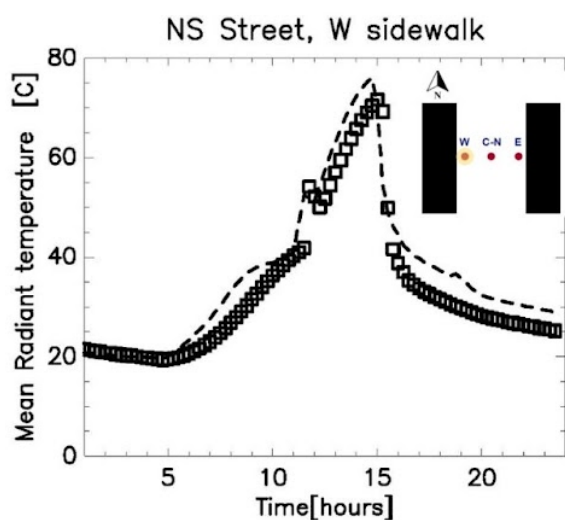
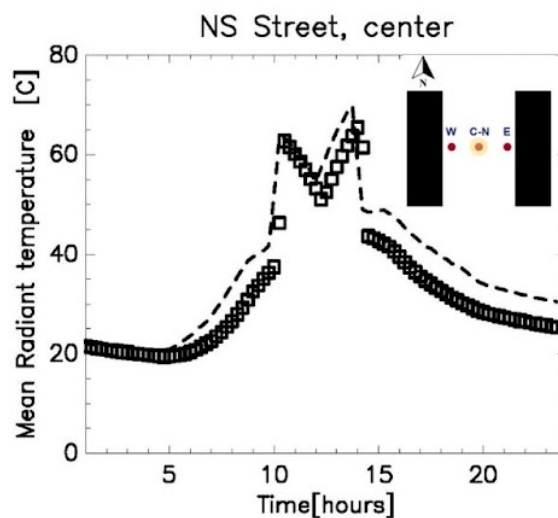
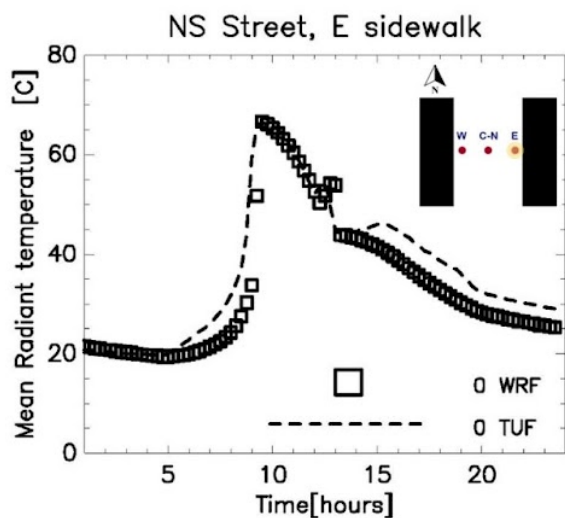


**Figure 1:** Two street directions (left: E-W canyon, right: N-S canyon) and pedestrian locations considered for Mean Radiant Temperature calculations.

124 The diurnal progression of the mean radiant temperature computed by this new model in BEP-BEM is subsequently  
125 compared with that obtained from TUF-Pedestrian, a more detailed three-dimensional model that has been evaluated against  
126 measurements (Lachapelle et al. 2022). TUF-Pedestrian is configured with identical input parameters and meteorological  
127 forcing, and with long canyons that approximate the two-dimensional BEP-BEM canyon geometry. The new model clearly  
128 captures the relevant details of the diurnal progression of MRT at all six locations (Fig. 2), with a mean absolute difference  
129 of 3.4 K, and a root mean square difference of 4.3 K across all locations. A comparison of the shortwave radiation loading on  
130 the pedestrian between the two models reveals excellent agreement (Appendix A Fig. A1, A2); thus, most of the model  
131 disagreement arises from differences between longwave loading on the pedestrian as a result of different methods for  
132 computation of surface temperature between the models. Overall, the new model of mean radiation temperature in  
133 BEP-BEM provides satisfactory results.





135 **Figure 2:** Comparison of diurnal variation of Mean Radiant Temperature (MRT) between the new model in BEP-BEM and  
136 TUF-Pedestrian for each of the six locations in Fig. 1.

## 137 2.2 Parameterize airflow variability in the urban canopy

138 Mesoscale models solve conservation equations for the three components of momentum. From these, it is possible to derive  
139 the spatially averaged wind velocity in each grid cell, at the grid resolution of the mesoscale model, commonly of the order  
140 of 300m-1km. The spatially averaged wind velocity in the urban canopy  $\langle V \rangle$ , close to the pedestrian height ( $\sim 2.5\text{m}$ ), is the  
141 square root of the sum of the spatial average of the two horizontal components  $u$ , and  $v$ , (neglecting the vertical component,  
142 which is usually at least one or two orders of magnitude smaller than the horizontal),

$$143 \langle V \rangle = \frac{1}{V_{air}} \sqrt{\left( \int_{V_{air}} u dV \right)^2 + \left( \int_{V_{air}} v dV \right)^2} \quad (2)$$

144 where here  $V_{air}$  is the volume of the grid cell occupied by air (e. g. without the buildings)

145 However, the wind velocity calculated in mesoscale models is different from the average wind speed that would be  
146 experienced by a person in the grid cell. This is better represented by the spatial average of the wind speed  $\langle U \rangle$  (e. g. the  
147 module of the vector), written as

$$148 \langle U \rangle = \frac{1}{V_{air}} \int_{V_{air}} \sqrt{u^2 + v^2} dV \quad (3)$$

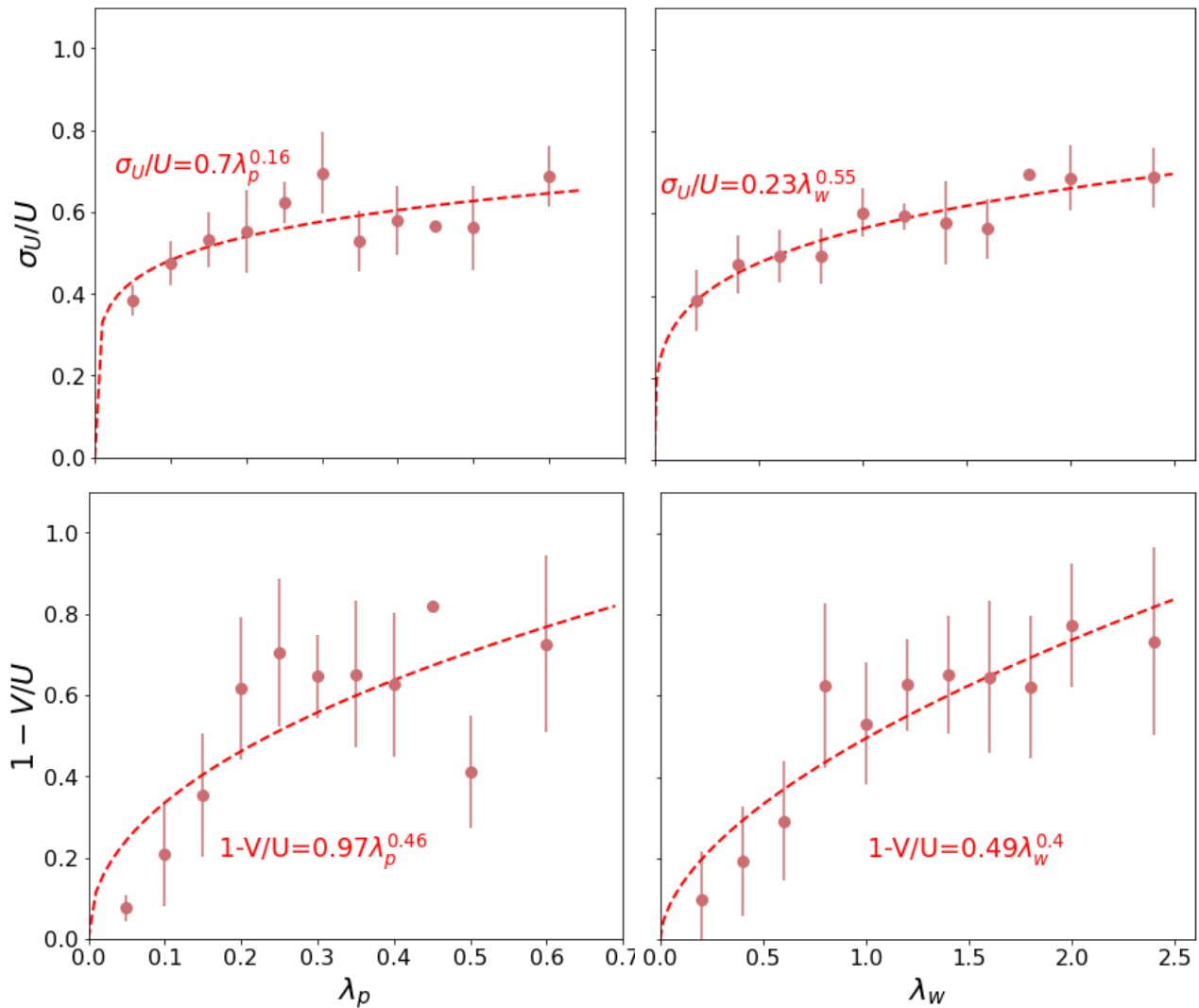
149 To assess the impact of airflow on human thermal comfort, the wind speed should be estimated from the wind velocity  
150 computed in the mesoscale models. Additionally, it is critical to parameterize and estimate the spatial variability of mean  
151 wind speed in the urban canopy. Accounting for these factors, the range of wind speed variability at the pedestrian level is  
152 estimated, which is critical for the quantification of spatial variability of outdoor thermal stress and comfort.

153 Here, we describe the parameterization of a) wind speed-to-velocity ratio and b) wind speed distribution, based on urban  
154 density parameters. Data from over 173 microscales CFD simulations of urban airflow are considered over realistic and  
155 idealized urban configurations, spanning a wide range of building plan area ( $\lambda_p$ ), frontal area ( $\lambda_f$ ), and wall area ( $\lambda_w$ ) densities  
156 representative of realistic urban neighborhoods in different types of cities. CFD simulations are conducted using 162  
157 large-eddy simulations (LES) and 11 Reynolds-averaged Navier–Stokes (RANS) schemes detailed in Appendix B.

158 Mean wind velocity  $\langle V \rangle$ , speed  $\langle U \rangle$  and its spatial standard deviation ( $\sigma_U$ ) are computed at a horizontal cross-section at  
159 pedestrian height for each CFD simulation and used for deriving parameterizations (Fig 3). An additional data point is added  
160 at  $\lambda_p=\lambda_w=0$ , ensuring that wind speed is equal to wind velocity, and its standard deviation is set to zero, for the non-urban  
161 case.



162



163 **Figure 3:** Relationship between  $1-\langle V \rangle / \langle U \rangle$  (bottom row), and  $\sigma_U / \langle U \rangle$  (top row), and two morphological parameters,  $\lambda_p$  (left column),  
 164 and  $\lambda_w$  (right column) based on the CFD simulations. Dots represent the average of the value among all the simulations that share the same  
 165 morphological parameter, and the vertical bar indicates the standard deviation. The dashed line and the formula indicate the best fit.

166

167 Parameterizations are derived (shown in Fig. 3) for two density parameters ( $\lambda_p = A_p / A_{tot}$ , and  $\lambda_w = A_w / A_{tot}$ , where  $A_p$  is the  
 168 area of the horizontal surface occupied by buildings, or the roof area,  $A_w$  is the area of vertical (wall) surfaces, and  $A_{tot}$  is  
 169 the total horizontal area). We find that  $\lambda_w$  better predicts mean wind speed and its spatial variability at the pedestrian height,  
 170 because it represents both horizontal and vertical heterogeneities in the urban canopy. Note that  $\lambda_f$  has not been included in





171 the study, given the difficulty to estimate it for real urban areas, and to translate it to the simplified 2D urban morphology  
172 used by BEP-BEM. In any case,  $\lambda_F$  is closely related to  $\lambda_w$ . Therefore, the following parameterizations are implemented at  
173 the pedestrian height (1.8m) as a function of the wall area density  $\lambda_w$

174

$$175 \langle U \rangle = \frac{\langle V \rangle}{1 - 0.49\lambda_w^{0.4}} \quad (4)$$

$$176 \sigma_U = \langle U \rangle (0.25\lambda_w^{0.55}) \quad (5)$$

177 We, therefore, assign three values of wind speed in each grid cell,

$$178 \langle speed \rangle_1 = \max(0.01, \langle U \rangle (1 - 0.25\lambda_w^{0.55}))$$

$$179 \langle speed \rangle_2 = \langle U \rangle \quad (6)$$

$$180 \langle speed \rangle_3 = \langle U \rangle (1 + 0.25\lambda_w^{0.55})$$

181 Note that here we consider the three values equally likely, in order to realistically span the range of possible values that the  
182 wind speed can take in each grid cell. Since UTCI has been designed for 10m wind speeds, a simple log law is used to  
183 rescale wind speed at 10m, before passing it to the UTCI routine.

### 184 2.3 Calculation of the thermal comfort index

185 To represent the subgrid spatial variability of air temperature, detailed CFD simulations are not available, so we simply used  
186 a variability of 1 degree Celsius, which we consider to be a conservative estimate of the spatial variability of air temperature  
187 over a spatial scale of the order of one km squared. Therefore, for each grid cell, we have three values for air temperature:

$$188 Temp_1 = Temp_{WRF} - 1$$

$$189 Temp_2 = Temp_{WRF} \quad (7)$$

$$190 Temp_3 = Temp_{WRF} + 1$$

191 Where  $Temp_{WRF}$  is the air temperature provided by WRF.

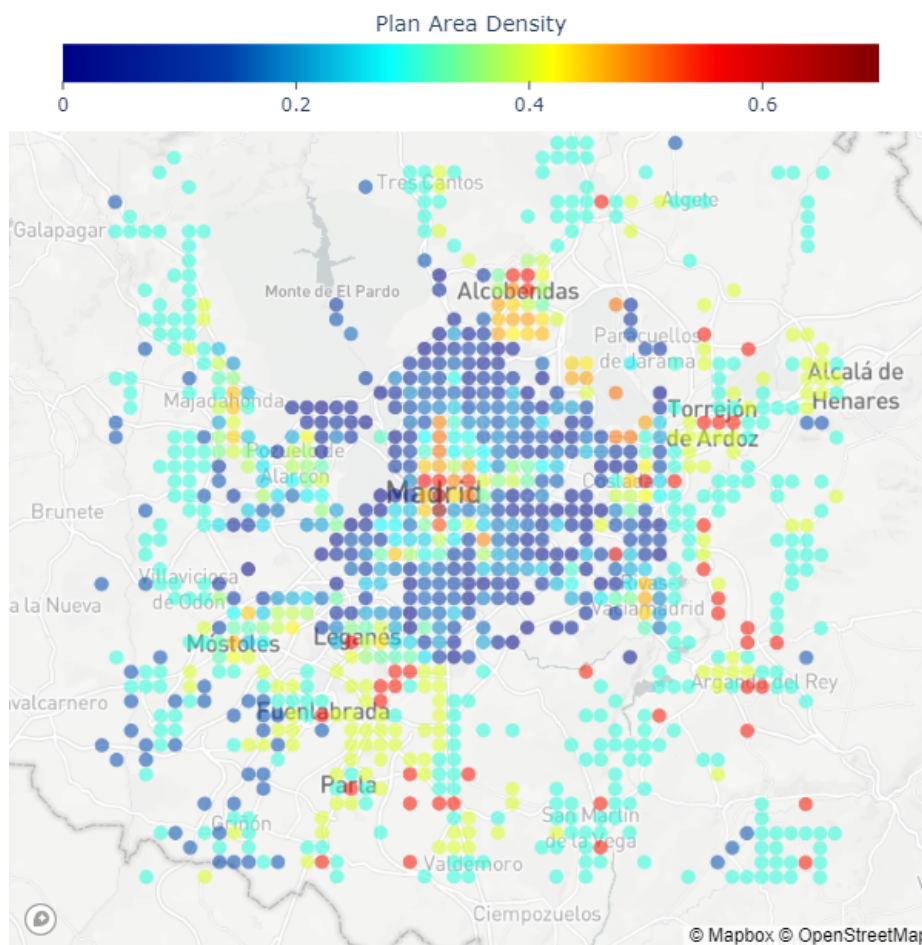
192 We therefore have, for each urban grid cell, *three* values of wind speed, *three* values of temperature, and *six* values of mean  
193 radiant temperature. No variability of the absolute humidity is considered, but the relative humidity is computed using the  
194 three values of air temperature.



195 Based on the variation of these climate variables, assumed uncorrelated, 54 possible combinations of the air temperature,  
196 mean radiant temperature, and wind speed values can be formed. For each one of these combinations, we calculate the  
197 corresponding SET or UTCI value. Based on the resulting distribution, we estimate the value of the 10th, 50th, and 90th  
198 percentile SET or UTCI for each grid square (at each output time).

### 199 3. Characterization of thermal comfort in regional-scale models: Madrid case

200 To illustrate the capabilities of the new scheme, a typical heat wave day in the city of Madrid (Spain) is simulated with WRF.  
201 Madrid is located on a plateau at 500-700m above sea level, in the middle of the Iberian Peninsula. It experiences hot  
202 summers, with frequent heat waves that are increasingly causing severe heat stress in the population, and it is therefore  
203 considered a relevant case study. Four nested domains have been used, with resolutions of 27,9,3, and 1km respectively. The  
204 city morphology (Fig. 4) is derived from high-resolution LIDAR data that covers most of the metropolitan area of Madrid  
205 (Martilli et al., 2022), while the morphology of the surrounding towns is determined based on Local Climate Zone maps  
206 (Brousse et al., 2016). It is also important to mention that the city is located on a hilly terrain, with higher elevations in the  
207 N-W part of the urban area (around 700m a.s.l.) dropping to 500m a.s.l. or less in the S-E. Moreover, there are two  
208 topographical depressions on the two sides of the city center, caused by the rivers Jarama and Manzanares (for a detailed  
209 description of the topography see also Martilli et al. 2022, where the same set-up was used). Other model configurations are  
210 the NOAH vegetation model for the non-urban grid points and the Bougeault and Lacarrere (1989) PBL scheme for  
211 turbulence parameterization. WRF coupled with BEP-BEM has previously been successfully used to simulate a heat wave  
212 period in Madrid (Salamanca et al., 2012). The period used in this paper is three days (14-16 July 2015). In particular, the  
213 analysis will focus on the 15th, when the maximum simulated temperature was above 40 Celsius. More information about  
214 the validation and a sensitivity study to select the optimal set-up can be found in Rodriguez-Sanchez (2020).



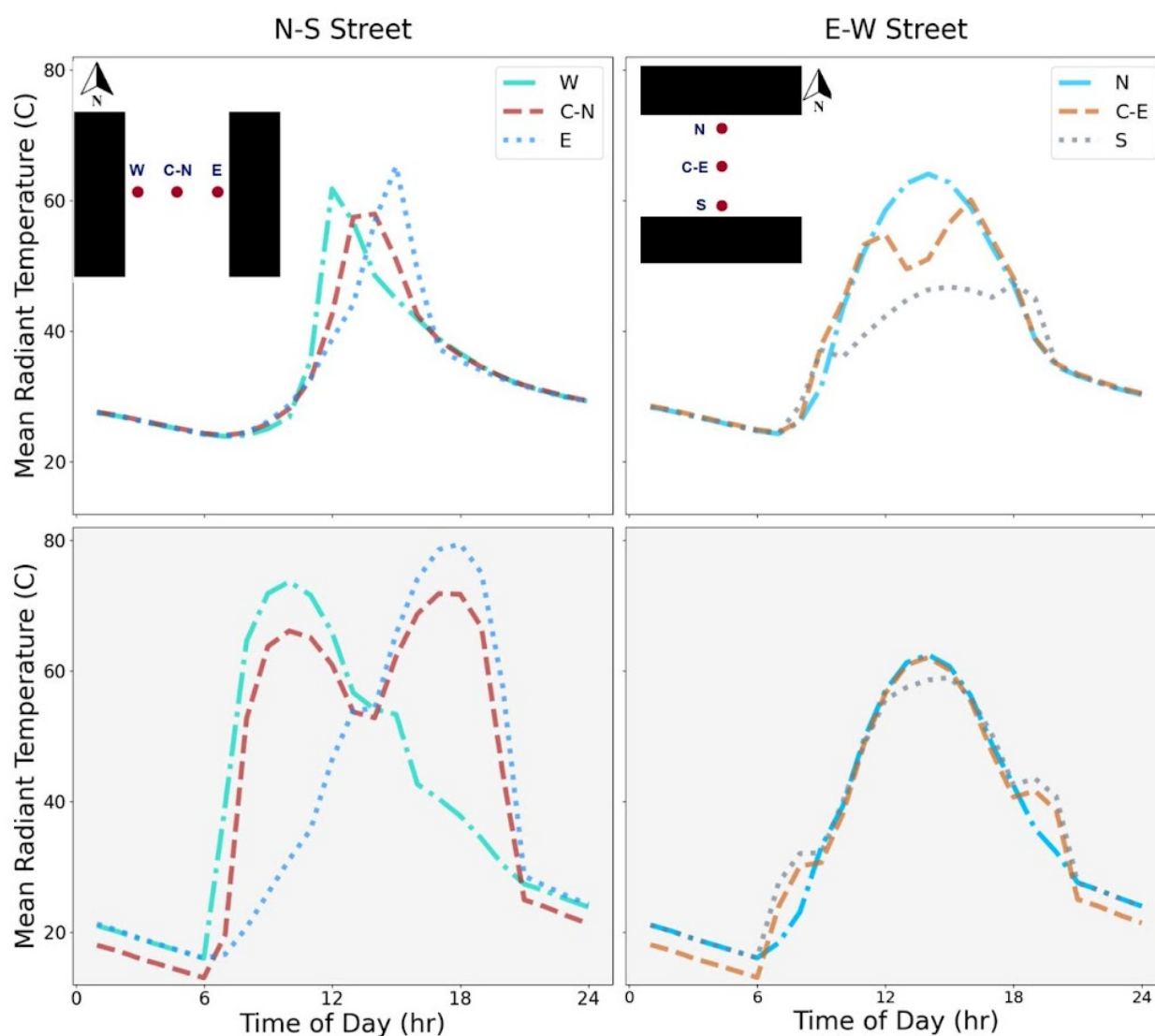
215

216 **Figure 4.** Map of the plan area building density over the Madrid region. The underlying map was created with Mapbox OpenStreetMap

### 217 3.1 Sub-grid scale variability of MRT and thermal comfort.

218 In order to understand how urban morphology affects the simulated heat stress, we focus on two grid points with very  
219 different urban morphology. One is located in the dense core of the city, with a building plan area density of  $\lambda_p = 0.69$ , and a  
220 height-to-width ratio (H/W) value of 1.6. The second is located in the southern part of the urban area, in a residential  
221 neighborhood with a much lower building density ( $\lambda_p = 0.2$ ) and a H/W=0.1.

222 In Figure 5, the diurnal evolution of the mean radiant temperature in the six points (three per street direction) is presented for  
223 the high urban density point and the low urban density point. During the daytime, the impact of the shadowing is clear, with  
224 reduced mean radiant temperature in the high-density point compared to the more exposed low-density. On the other hand,  
225 during nighttime, the reduced sky-view factor in the high-density point slows down the cooling compared to the more open  
226 low-density location.



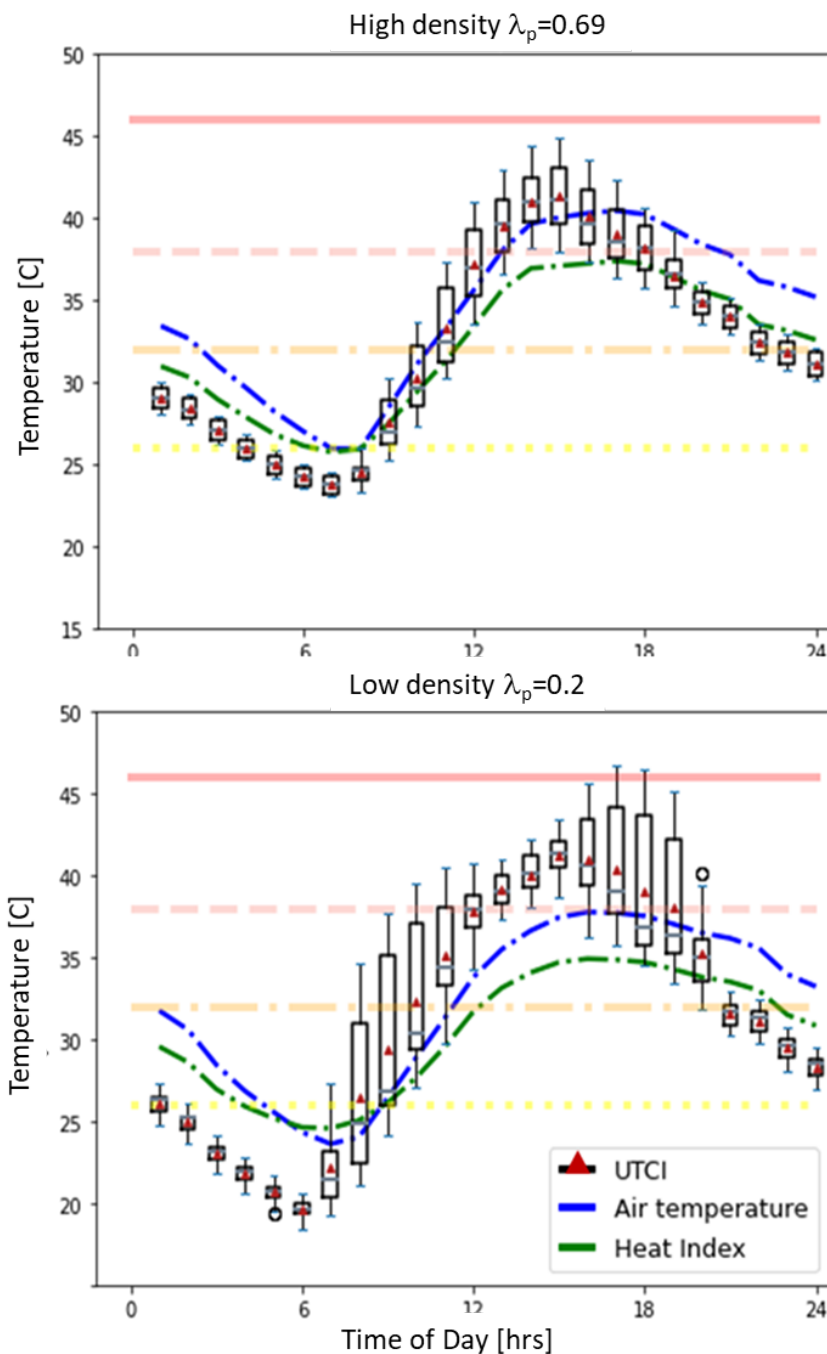
227

228 **Figure 5.** Diurnal evolution of MRT for 6 points in the urban canopy. The top row (white background) corresponds to a grid with the  
229 highest building density in the center of Madrid ( $\lambda_p = 0.69$ ) while the bottom row (with grey background) shows MRT in a low-density  
230 neighborhood ( $\lambda_p = 0.19$ ). The left column is for an N-S street, while the right column shows an E-W street.

231 This behavior helps to explain the heat stress index (Figure 6). The air temperature indicates hotter values both during the  
232 day and the night in the high urban density point compared to the low-density location. The Heat Index, which considers air



233 temperature and humidity only, and does not include mean radiant temperature or wind, shows the same tendency. On the  
234 other hand, the UTCI behavior communicates a different and more complete result. In the low-density neighborhood, more  
235 exposed to the sun, the UTCI shows a stronger sub-grid spatial variability, in particular during the morning and afternoon,  
236 with the potential for stronger heat stress than in the high-density neighborhood. During nighttime, the spatial variability is  
237 reduced, due to reduced MRT variation as the shadowing effect disappears, and higher UTCI values are found at the high  
238 urban density location. This difference in behavior between the two locations can be seen also in Fig. 7, where the fractions  
239 of the 10th percentile of UTCI values (i.e. representative of one of the coolest spots in the grid cell) and the 90th percentile  
240 (i.e., one of the hottest) in the different heat stress regimes are shown for the two points. Here we can see that in the  
241 low-density urban point, the cool location is in a comfortable UTCI range most of the time, while the hot (90th percentile  
242 UTCI) subgrid location is under stress most of the time. On the other hand, less variability is present in the high-density  
243 neighborhood, with fewer extreme values, and most of the time in the strong or moderate heat stress regime for both the cool  
244 and hot locations within the grid square. This kind of detail is not available from the Heat index distribution which does not  
245 account for the mean radiant temperature, wind, or their variabilities (Fig. 8).

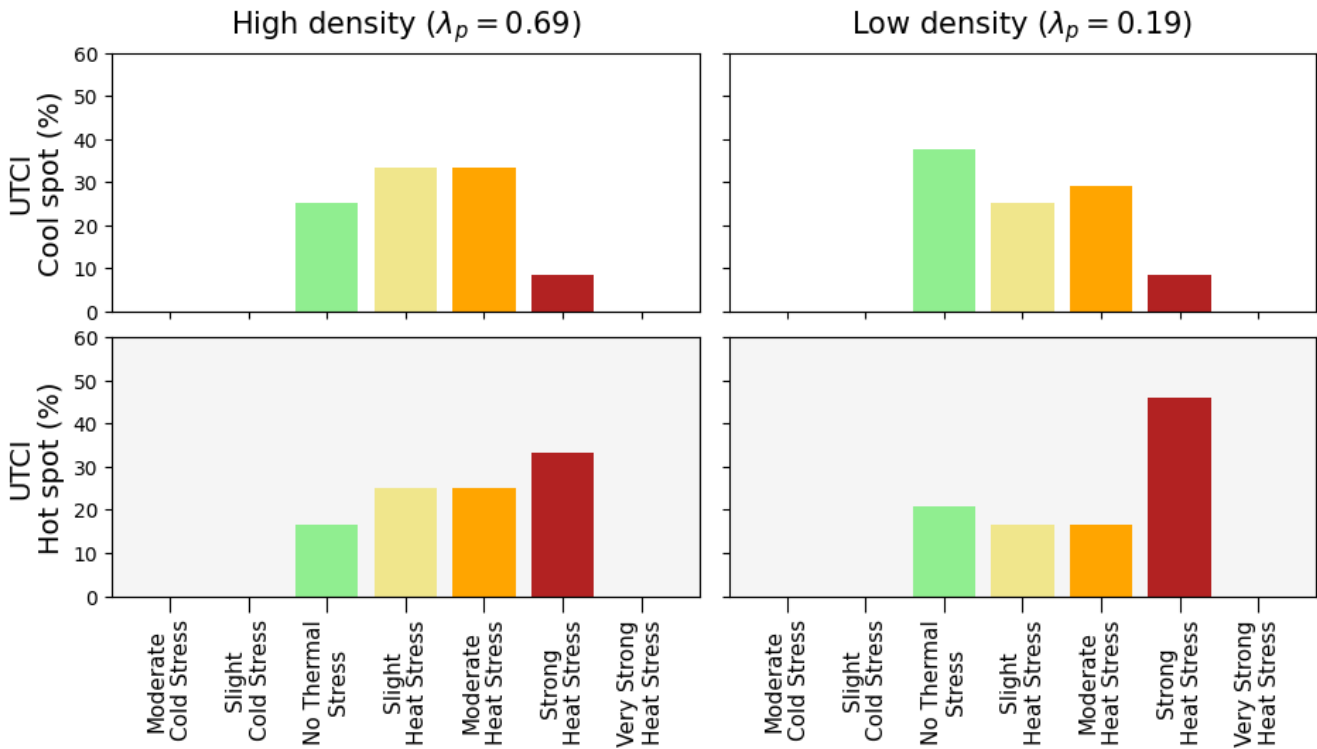


246

247 **Figure 6.** Diurnal evolution of UTCI compared with 2-m air temperature and heat index calculated from air temperature and relative  
248 humidity at each grid point). The UTCI boxplot at each hour represents the subgrid-scale distribution calculated based on 6 MRT, 3 wind  
249 speeds, and 3 air temperature values (54 combinations in total). The horizontal lines represent the thermal comfort zones for UTCI (i.e.



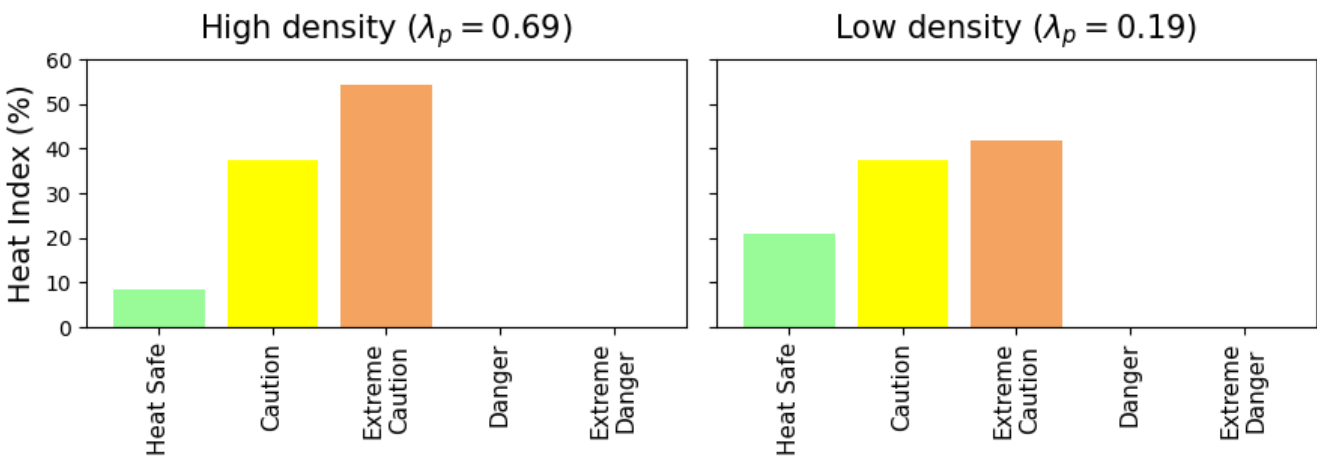
250 above +46C: extreme heat stress; +38 to +46: very strong heat stress; +32 to +38: strong heat stress; +26 to +32: moderate heat stress; and  
251 +9 to +26: no thermal stress).



252

253

254 **Figure 7.** From top to bottom, the frequency of UTCI class over a 24-hour period, for a subgrid location that is cooler (i.e. 10th percentile  
 255 of UTCI in the urban canopy, top), and for a subgrid location that is hotter (i.e. 90th percentile of UTCI in the urban canopy, bottom), for  
 256 the high-density (left) and low-density (right) points.



257

258

**Figure 8.** same as Figure 7, but for the Heat Index



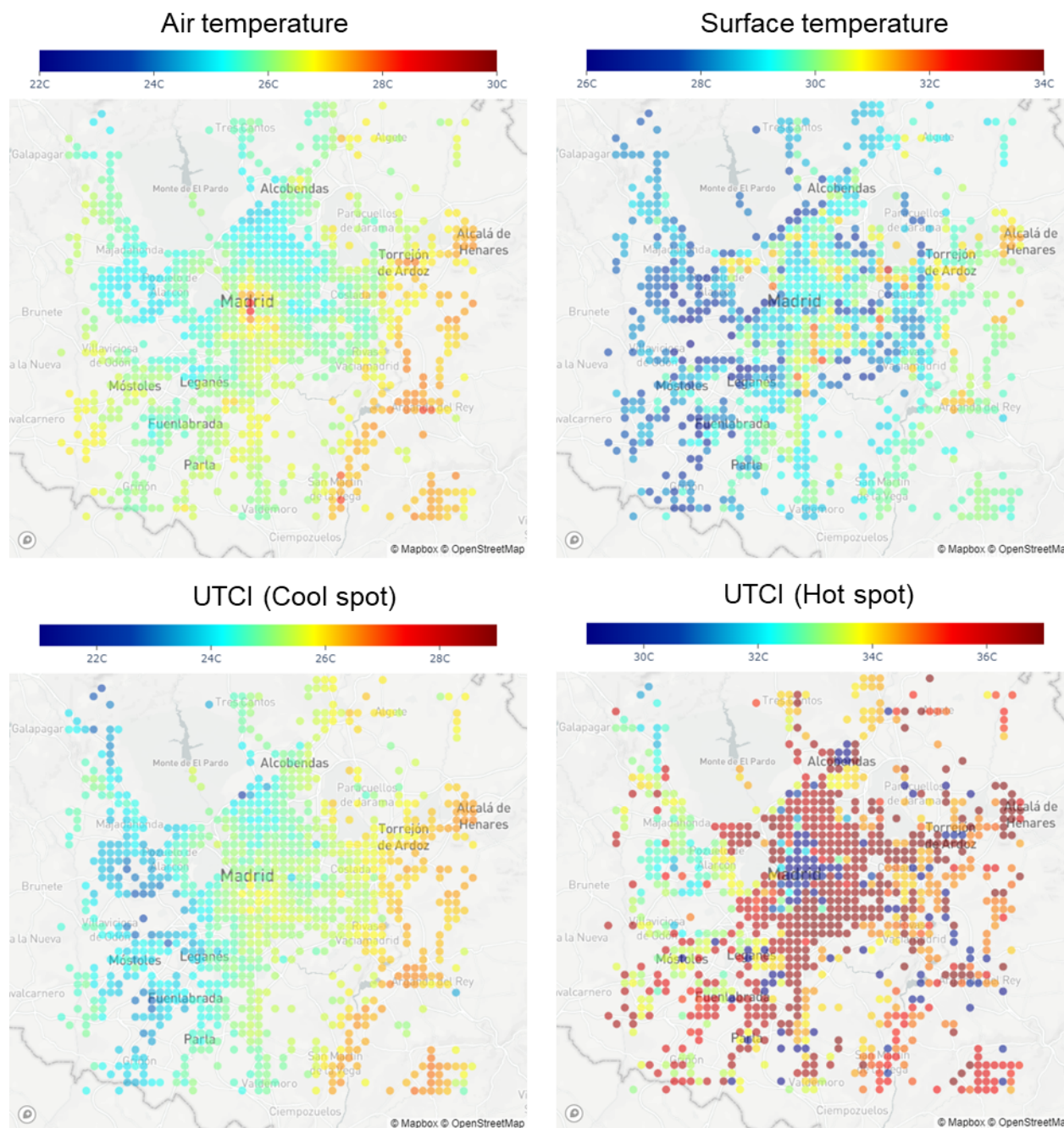


259

### 260 3.2 City-scale maps of outdoor thermal comfort and heat stress indicators.

261 The previous analysis helps to understand the spatial distribution of the different variables presented in Fig. 9 at 10 and 16  
262 UTC (note that Madrid is at Longitude 3W, so UTC is essentially equal to solar time). The distribution of 2m air temperature  
263 at 9 UTC shows a hot region in the dense city center, with cooler areas in the less dense regions around it. This effect is due  
264 to the fact that in the dense region, the reduced sky-view factor of the streets (high H/W), as well as the larger thermal  
265 storage in the buildings, reduce the nocturnal cooling, and increase the vertical mixing in that part of the city compared to the  
266 surroundings. Such a difference is still visible in the morning. The higher temperatures in the S-E part of the urban area, and  
267 cool temperatures in the N-W are the result of the topographical differences. The spatial distribution of air temperature is  
268 qualitatively similar to the spatial distribution of the 10-percentile of UTCI (e. g. the cool spot in the grid cell), even if the  
269 differences between the center and the surrounding urban areas are not as intense as for 2m air temperature. On the other  
270 hand, the 90-percentile map (hot spot), shows a completely different pattern, due to the fact that in the city center, at that  
271 time of the day, the whole street is still in the shadow, while in the surrounding, less dense urban areas there are points  
272 completely exposed to the sun. As a comparison, the map of surface temperature (a variable often used to represent the  
273 spatial distribution of heat in cities) as seen from a satellite, i.e. based only on a weighted average of roof, street, and  
274 vegetation temperatures (see full equations in Martilli et al. 2021), does not show a clear pattern, and it is uncorrelated with  
275 the other maps. This is a clear indication that this variable should not be used for the assessment of the heat hazard or heat  
276 stress in urban areas.

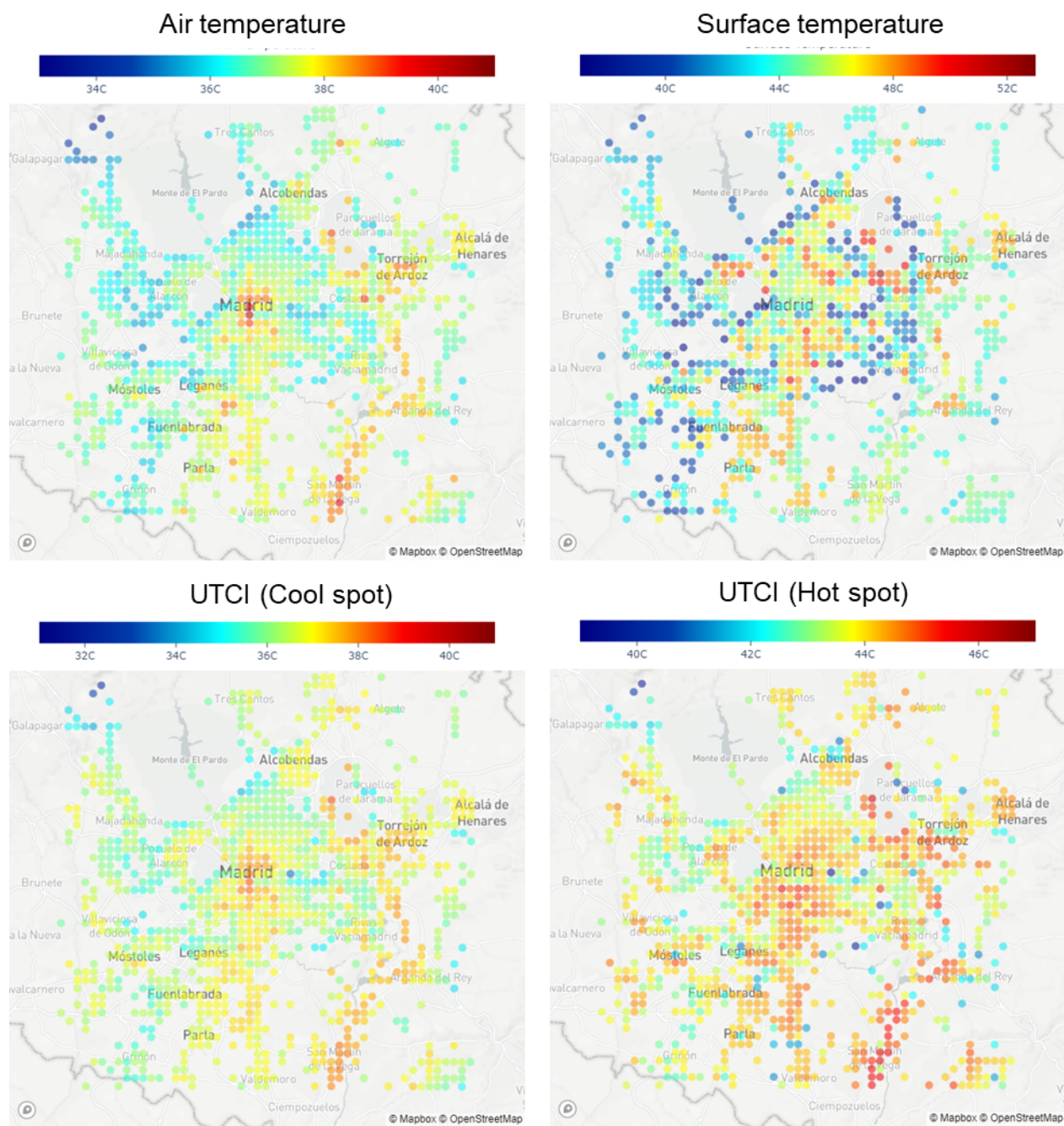
277 At 1600 UTC the air temperature shows again higher values in the city center, lower in the urban surroundings, and a  
278 gradient from hotter S-E at lower elevations to cooler N-W at higher elevations (Fig. 10). Such a tendency is present also for  
279 the 10th percentile (cool spot), but with less variability. The 90th percentile map (hot spot) indicates that the area with  
280 elevated heat stress extends well beyond the city center, including lower-density regions that, even if they have lower air  
281 temperatures, are fully exposed to the sun. Finally, as it was the case for 09000 UTC, the surface temperatures have a map  
282 uncorrelated with neither the air temperatures nor the UTCI maps.



283  
284 **Figure 9.** Spatial maps at 0900 UTC for 2-m air temperature (top left), surface temperature (top right), UTCI cool spot e. g. the 10  
285 percentile of UTCI captured in the urban canopy model (bottom left), and UTCI hot spot e. g. 90 percentile of UTCI in the urban canopy  
286 (bottom right). Surface temperature is equivalent to that seen by a nadir-view satellite sensor (i.e., an area-weighted average of canopy  
287 ground temperature, roof temperature, and vegetation temperature in non-urban fractions is considered). The underlying maps were created  
288 with Mapbox OpenStreetMap



289



290

291

Figure 10. Same as Figure 9, but at 1600 UTC.

#### 292 4. Conclusions



293 A new parameterization to quantify intra-neighborhood heat stress variability in urban areas using a mesoscale model is  
294 presented. This approach is based on two primary developments: 1) calculation of mean radiant temperature at several  
295 locations within the idealized urban morphology used by the urban canopy model BEP-BEM; and 2) parameterization of  
296 mean wind speed and its sub-grid spatial variability as a function of the local urban morphology and the mean wind velocity  
297 computed by the WRF mesoscale model, using relations developed from a large suite of CFD simulations over a range of  
298 realistic and idealized urban neighborhoods. The components of the new parameterization have been validated against  
299 microscale model results. From this approach the sub-grid variability of a heat stress index (i.e. UTCI or SET) can be  
300 computed for every grid point, permitting quantification of the heat exposure at both cool and hot locations within each grid  
301 square at each time.

302 The new parameterization has been implemented in the multilayer scheme BEP-BEM in WRF and used to simulate a  
303 heatwave day over Madrid (Spain) as proof of concept. The results of this initial application demonstrate the following:

- 304 I. The new parameterization gives information that is more suitable for the evaluation of heat stress than the air  
305 temperature, being based on an index (UTCI or SET) that also combines air humidity, wind speed, and mean radiant  
306 temperature.
- 307 II. The new parameterization provides substantively more information than air temperature alone (or any other index  
308 that does not account for the mean radiant temperature). It provides information about the sub-grid variability (such  
309 that heat stress in both cool and hot locations in each grid square is quantified). To our knowledge, this has never  
310 been done before with a mesoscale model.
- 311 III. The results for the investigated case, indicate a strong intraurban variability, both in air temperature and UTCI  
312 values, that can be linked to the differences in urban morphology and elevation above sea level. The ability to assess  
313 the differential impacts of urban morphology on heat stress is key to the provision of guidance for urban planning  
314 strategies that mitigate urban overheating.
- 315 IV. Nadir-view surface temperature (i.e., as seen from a satellite-mounted remote sensor) is poorly correlated with both  
316 air temperature and UTCI maps, indicating that, despite its ubiquitous use at present, it is unlikely to be an adequate  
317 metric for heat impact assessment studies.

318 Finally, we consider that this new development introduces a new methodology for deploying mesoscale models to assess  
319 urban overheating mitigation strategies.

320



321

322 ***Code Availability***

323 The code of WRF-comfort can be obtained here:

324 <https://doi.org/10.5281/zenodo.7951433>

325 The results of the simulation over Madrid shown in the manuscript are stored here:

326 <https://zenodo.org/record/8199017>

327

328 ***Competing interests***

329 The authors declare that they have no conflict of interest

330



331

## 332 References

- 333 Bougeault, P. and Lacarrere, P.: Parameterization of Orography-Induced Turbulence in a Mesobeta--Scale Model, *Mon.*  
334 *Weather Rev.*, 117, 1872–1890, [https://doi.org/10.1175/1520-0493\(1989\)117<1872:POOITI>2.0.CO;2](https://doi.org/10.1175/1520-0493(1989)117<1872:POOITI>2.0.CO;2), 1989.
- 335 Broadbent, A. M., Krayenhoff, E. S., and Georgescu, M.: The motley drivers of heat and cold exposure in 21st century US  
336 cities, *Proc. Natl. Acad. Sci. U. S. A.*, 117, 21108–21117, <https://doi.org/10.1073/pnas.2005492117>, 2020.
- 337 Brousse, O., Martilli, A., Foley, M., Mills, G., and Bechtel, B.: WUDAPT, an efficient land use producing data tool for  
338 mesoscale models? Integration of urban LCZ in WRF over Madrid, *Urban Climate*, 17, 116–134,  
339 <https://doi.org/10.1016/j.uclim.2016.04.001>, 2016.
- 340 Brown, M. J., Lawson, R. E., DeCroix, D. S., Lee, R. L., and Others: Comparison of centerline velocity measurements  
341 obtained around 2D and 3D building arrays in a wind tunnel, *Int. Soc. Environ. Hydraulics*, Tempe, AZ, 5, 495, 2001.
- 342 Coceal, O., Dobre, A., Thomas, T. G., and Belcher, S. E.: Structure of turbulent flow over regular arrays of cubical  
343 roughness, *J. Fluid Mech.*, 589, 375–409, <https://doi.org/10.1017/S002211200700794X>, 2007.  
344 Structure of turbulent flow over regular arrays of cubical roughness. *Journal of Fluid Mechanics*, 589, 375-409.  
345 (doi:10.1017/S002211200700794X <<http://dx.doi.org/10.1017/S002211200700794X>>). , 2007.
- 346 Franke, J., Hellsten, A., Schlünzen, H., and Carissimo, B.: The Best Practise Guideline for the CFD simulation of flows in  
347 the urban environment: an outcome of COST 732, in: *The Fifth International Symposium on Computational Wind*  
348 *Engineering (CWE2010)*, 1–10, 2010.
- 349 Frigo, M. and Johnson, S. G.: FFTW: an adaptive software architecture for the FFT, in: *Proceedings of the 1998 IEEE*  
350 *International Conference on Acoustics, Speech and Signal Processing, ICASSP '98 (Cat. No.98CH36181)*, 1381–1384 vol.3,  
351 <https://doi.org/10.1109/ICASSP.1998.681704>, 1998.
- 352 Gagge, A. P., Fobelets, A. P., Berglund, L., and Others: A standard predictive index of human response to the thermal  
353 environment, *ASHRAE Trans.*, 92, 709–731, 1986.
- 354 Geletič, J., Lehnert, M., Savić, S., and Milošević, D.: Modelled spatiotemporal variability of outdoor thermal comfort in  
355 local climate zones of the city of Brno, Czech Republic, *Sci. Total Environ.*, 624, 385–395,  
356 <https://doi.org/10.1016/j.scitotenv.2017.12.076>, 2018.
- 357 Giannaros, T. M., Lagouvardos, K., Kotroni, V., & Matzarakis, A. (2018). Operational forecasting of  
358 human-biometeorological conditions. *International journal of biometeorology*, 62, 1339-1343.
- 359 Giannaros, C., Agathangelidis, I., Papavasileiou, G., Galanaki, E., Kotroni, V., Lagouvardos, K., ... & Matzarakis, A. (2023).  
360 The extreme heat wave of July–August 2021 in the Athens urban area (Greece): Atmospheric and human-biometeorological



- 361 analysis exploiting ultra-high resolution numerical modeling and the local climate zone framework. *Science of The Total*  
362 *Environment*, 857, 159300.
- 363 Höppe, P.: The physiological equivalent temperature - a universal index for the biometeorological assessment of the thermal  
364 environment, *Int. J. Biometeorol.*, 43, 71–75, <https://doi.org/10.1007/s004840050118>, 1999.
- 365 Jendritzky, G., de Dear, R., and Havenith, G.: UTCI—Why another thermal index?, *Int. J. Biometeorol.*, 56, 421–428,  
366 <https://doi.org/10.1007/s00484-011-0513-7>, 2012.
- 367 Jin, L., Schubert, S., Fenner, D., Salim, M. H., and Schneider, C.: Estimation of mean radiant temperature in cities using an  
368 urban parameterization and building energy model within a mesoscale atmospheric model, *Meteorol. Z.*, 31, 31–52, 2022.
- 369 Kracht, O., Santiago, J., Martin, F., Piersanti, A., Cremona, G., Righini, G., Vitali, L., Delaney, K., Basu, B., Ghosh, B.,  
370 Spangl, W., Brendle, C., Latikka, J., Kousa, A., Pärjälä, E., Meretoja, M., Malherbe, L., Letinois, L., Beauchamp, M.,  
371 Lenartz, F., Hutsemekers, V., Nguyen, L., Hoogerbrugge, R., Eneroth, K., Silvergren, S., Hooyberghs, H., Viaene, P.,  
372 Maiheu, B., Janssen, S., Roet, D. and Gerboles, M., Spatial representativeness of air quality monitoring sites: Outcomes of  
373 the FAIRMODE/AQUILA intercomparison exercise, EUR 28987 EN, Publications Office of the European Union,  
374 Luxembourg, 2017, ISBN 978-92-79-77218-4, doi:10.2760/60611, JRC108791.
- 375 Krayenhoff, E. S., Moustauoui, M., Broadbent, A. M., Gupta, V., and Georgescu, M.: Diurnal interaction between urban  
376 expansion, climate change and adaptation in US cities, *Nat. Clim. Chang.*, 8, 1097–1103,  
377 <https://doi.org/10.1038/s41558-018-0320-9>, 2018.
- 378 Lemonsu, A., Viguié, V., Daniel, M., and Masson, V.: Vulnerability to heat waves: Impact of urban expansion scenarios on  
379 urban heat island and heat stress in Paris (France), *Urban Climate*, 14, 586–605, <https://doi.org/10.1016/j.uclim.2015.10.007>,  
380 2015.
- 381 Leroyer, S., Bélaïr, S., Spacek, L., and Gultepe, I.: Modelling of radiation-based thermal stress indicators for urban numerical  
382 weather prediction, *Urban Climate*, 25, 64–81, <https://doi.org/10.1016/j.uclim.2018.05.003>, 2018.
- 383 Lu, J., Nazarian, N., Hart, M. A., Krayenhoff, E. S., and Martilli, A.: Novel geometric parameters for assessing flow over  
384 realistic versus idealized urban arrays, *Journal of Advances in Modeling Earth Systems*, 2022.
- 385 Lu, J., Nazarian, N., Hart, M. A., Krayenhoff, E. S., and Martilli, A.: Describing building height variability in urban canopy  
386 parameterizations, *Geoscientific Model Development*, 2023.
- 387 Maronga, B., Banzhaf, S., Burmeister, C., Esch, T., Forkel, R., Fröhlich, D., Fuka, V., Gehrke, K. F., Geletič, J., Giersch, S.,  
388 Gronemeier, T., Groß, G., Heldens, W., Hellsten, A., Hoffmann, F., Inagaki, A., Kadasch, E., Kanani-Sühring, F., Ketelsen,  
389 K., Khan, B. A., Knigge, C., Knoop, H., Krč, P., Kurppa, M., Maamari, H., Matzarakis, A., Mauder, M., Pallasch, M., Pavlik,  
390 D., Pfafferott, J., Resler, J., Rissmann, S., Russo, E., Salim, M., Schrempf, M., Schwenkel, J., Seckmeyer, G., Schubert, S.,



- 391 Sühring, M., von Tils, R., Vollmer, L., Ward, S., Witha, B., Wurps, H., Zeidler, J., and Raasch, S.: Overview of the PALM  
392 model system 6.0, *Geosci. Model Dev.*, 13, 1335–1372, <https://doi.org/10.5194/gmd-13-1335-2020>, 2020.
- 393 Martilli, A., Clappier, A., and Rotach, M. W.: An Urban Surface Exchange Parameterisation for Mesoscale Models,  
394 *Bound.-Layer Meteorol.*, 104, 261–304, <https://doi.org/10.1023/A:1016099921195>, 2002.
- 395 Martilli, A., Sánchez, B., Santiago, J. L., Rasilla, D., Pappaccogli, G., Allende, F., Martín, F., Roman-Cascón, C., Yagüe, C.,  
396 and Fernández, F.: Simulating the pollutant dispersion during persistent Wintertime thermal Inversions over urban areas. The  
397 case of Madrid, *Atmos. Res.*, 270, 106058, <https://doi.org/10.1016/j.atmosres.2022.106058>, 2022.
- 398 Matzarakis, A., Rutz, F., Mayer, H., 2007. Modelling radiation fluxes in simple and complex environments—application of  
399 the RayMan model. *Int. J. Biometeorol.* 51, 323–334. <https://doi.org/10.1007/s00484-006-0061-8>.
- 400 Nazarian, N., Fan, J., Sin, T., Norford, L., and Kleissl, J.: Predicting outdoor thermal comfort in urban environments: A 3D  
401 numerical model for standard effective temperature, *Urban climate*, 2017.
- 402 Nazarian, N., Acero, J. A., and Norford, L.: Outdoor thermal comfort autonomy: Performance metrics for climate-conscious  
403 urban design, *Build. Environ.*, 155, 145–160, <https://doi.org/10.1016/j.buildenv.2019.03.028>, 2019.
- 404 Nazarian, N., Krayenhoff, E. S., and Martilli, A.: A one-dimensional model of turbulent flow through “urban” canopies  
405 (MLUCM v2.0): updates based on large-eddy simulation, *Geosci. Model Dev.*, 13, 937–953,  
406 <https://doi.org/10.5194/gmd-13-937-2020>, 2020.
- 407 Nazarian, N., Krayenhoff, E. S., Bechtel, B., Hondula, D. M., Paolini, R., Vanos, J., Cheung, T., Chow, W. T. L., de Dear, R.,  
408 Jay, O., Lee, J. K. W., Martilli, A., Middel, A., Norford, L. K., Sadeghi, M., Schiavon, S., and Santamouris, M.: Integrated  
409 assessment of urban overheating impacts on human life, *Earths Future*, 10, <https://doi.org/10.1029/2022ef002682>, 2022.
- 410 Piacsek, S. A. and Williams, G. P.: Conservation properties of convection difference schemes, *J. Comput. Phys.*, 6, 392–405,  
411 [https://doi.org/10.1016/0021-9991\(70\)90038-0](https://doi.org/10.1016/0021-9991(70)90038-0), 1970.
- 412 Pigliautile, I., Pisello, A. L., and Bou-Zeid, E.: Humans in the city: Representing outdoor thermal comfort in urban canopy  
413 models, *Renewable Sustainable Energy Rev.*, 133, 110103, <https://doi.org/10.1016/j.rser.2020.110103>, 2020.
- 414 Rodriguez-Sanchez, 2020, Simulación de olas de calor en la ciudad de Madrid, Master Thesis, Universidad Complutense de  
415 Madrid,  
416 [https://www.researchgate.net/publication/353350538\\_Simulacion\\_de\\_olas\\_de\\_calor\\_en\\_la\\_ciudad\\_de\\_Madrid#fullTextFile](https://www.researchgate.net/publication/353350538_Simulacion_de_olas_de_calor_en_la_ciudad_de_Madrid#fullTextFile)  
417 Content
- 418 Salamanca, F., Krpo, A., Martilli, A., and Clappier, A.: A new building energy model coupled with an urban canopy  
419 parameterization for urban climate simulations—part I. formulation, verification, and sensitivity ..., *Theoretical and applied*,  
420 2010.





421 Salamanca, F., Martilli, A., and Yagüe, C.: A numerical study of the Urban Heat Island over Madrid during the DESIREX  
422 (2008) campaign with WRF and an evaluation of simple mitigation strategies, *International Journal of*, 2012.

423 Santiago, J.L., Rivas, E., Sanchez, B., Buccolieri, R. and Martin, F., 2017. The impact of planting trees on NOx  
424 concentrations: The case of the Plaza de la Cruz neighborhood in Pamplona (Spain). *Atmosphere*, 8(7), p.131.  
425 <https://doi.org/10.3390/atmos8070131>

426 Santiago, J.L., Sanchez, B., Quaassdorff, C., de la Paz, D., Martilli, A., Martín, F., Borge, R., Rivas, E., Gómez-Moreno, F.J.,  
427 Díaz, E. and Artiñano, B., Yagüe, C. and Vardoulakis, S., 2020. Performance evaluation of a multiscale modelling system  
428 applied to particulate matter dispersion in a real traffic hot spot in Madrid (Spain). *Atmos. Pollut. Res.*, 11 (1), pp. 141-155.  
429 <https://doi.org/10.1016/j.apr.2019.10.001>

430 Sanchez, B., Santiago, J.L., Martilli, A., Martin, F., Borge, R., Quaassdorff, C. and de la Paz, D, 2017. Modelling NOx  
431 concentrations through CFD-RANS in an urban hot-spot using high resolution traffic emissions and meteorology from a  
432 mesoscale model. *Atmos. Environ.*, 163, pp. 155-165. <https://doi.org/10.1016/j.atmosenv.2017.05.022>

433 Sanchez, B., Santiago, J.L., Martilli, A., Palacios, M., Núñez, L., Pujadas, M. and Fernández-Pampillón, J., 2021. NOx  
434 depolluting performance of photocatalytic materials in an urban area - Part II: assessment through computational fluid  
435 dynamics simulations. *Atmos. Environ.*, 246 (2021), p. 118091. <https://doi.org/10.1016/j.atmosenv.2020.118091>

436 Skamarock, W. C., Klemp, J. B., Dudhia, J., Gill, D. O., Liu, Z., Berner, J., Wang, W., Powers, J. G., Duda, M. G., Barker, D.  
437 M., and Others: A description of the advanced research WRF model version 4, National Center for Atmospheric Research:  
438 Boulder, CO, USA, 145, 550, 2019.

439 Tuholske, C., Caylor, K., Funk, C., Verdin, A., Sweeney, S., Grace, K., Peterson, P., and Evans, T.: Global urban population  
440 exposure to extreme heat, *Proc. Natl. Acad. Sci. U. S. A.*, 118, <https://doi.org/10.1073/pnas.2024792118>, 2021.

441 Zhang, J., Li, Z., and Hu, D.: Effects of urban morphology on thermal comfort at the micro-scale, *Sustainable Cities and*  
442 *Society*, 86, 104150, <https://doi.org/10.1016/j.scs.2022.104150>, 2022.

443 Zhao, L., Oleson, K., Bou-Zeid, E., Krayenhoff, E. S., Bray, A., Zhu, Q., Zheng, Z., Chen, C., and Oppenheimer, M.: Global  
444 multi-model projections of local urban climates, *Nat. Clim. Chang.*, <https://doi.org/10.1038/s41558-020-00958-8>, 2021.

445

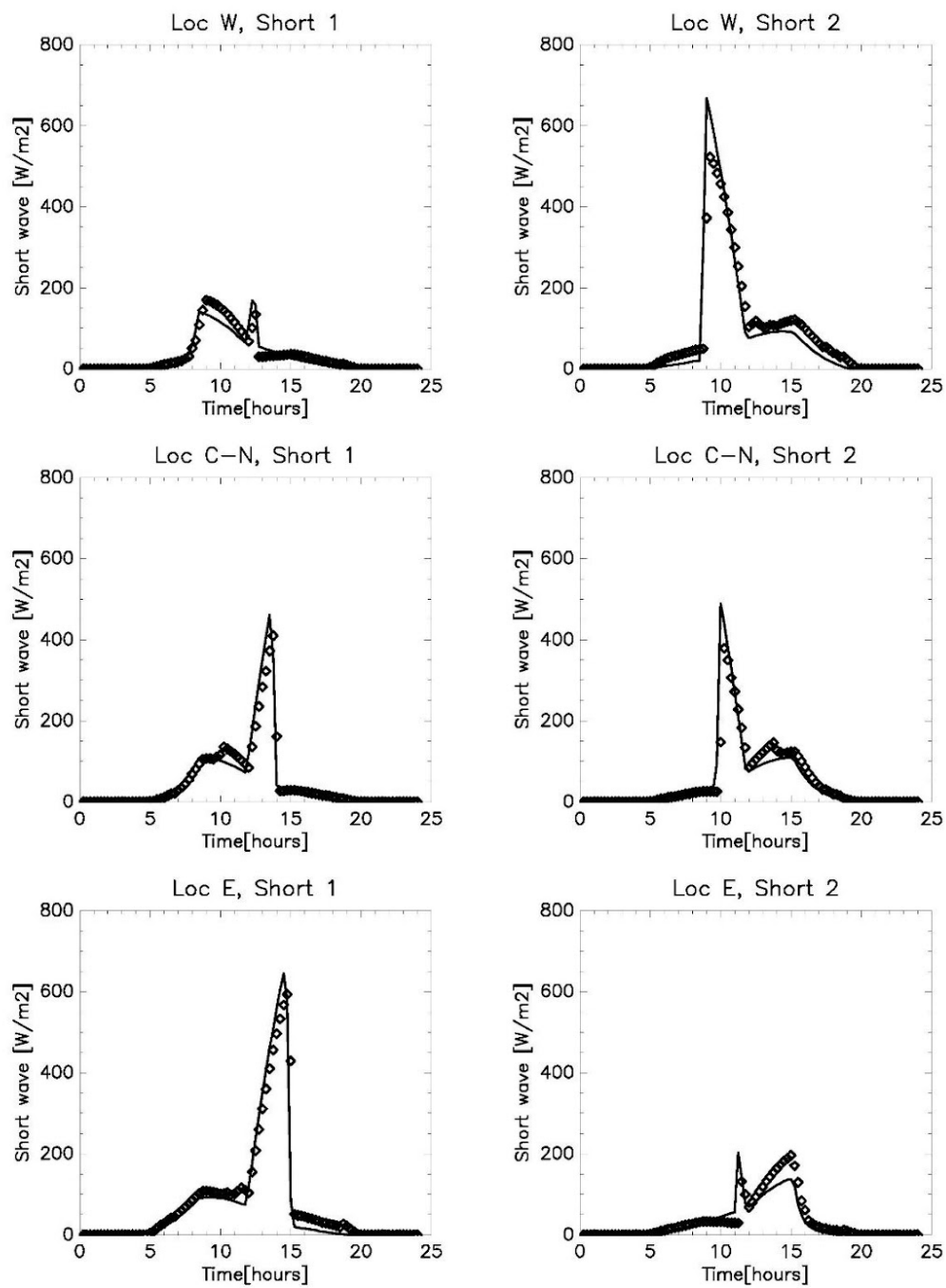
446



447

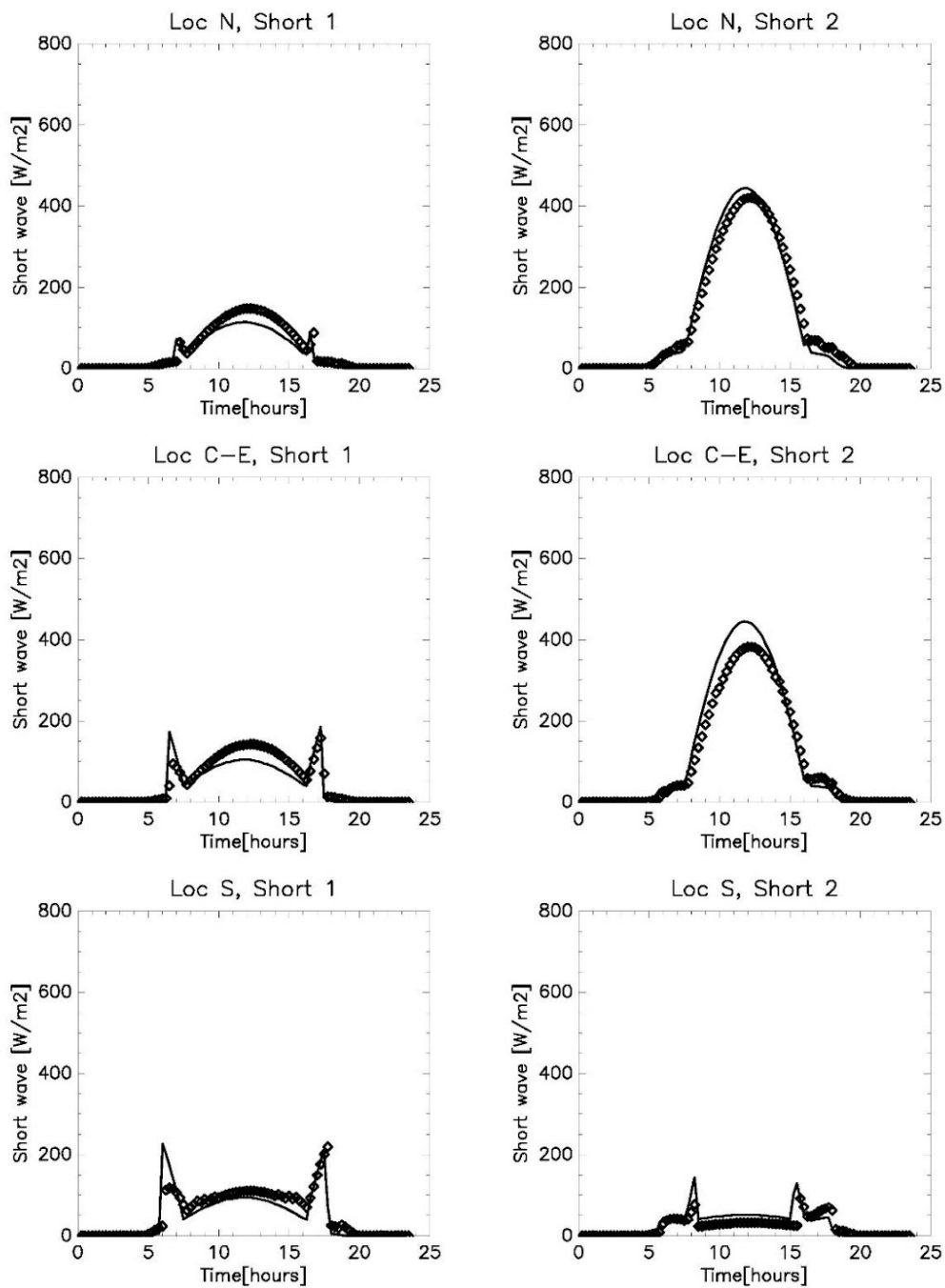
448 Appendix A. Comparison of Short wave calculation in BEP-BEM and TUF-pedestrian.

449 Short wave radiation is an essential component of the MRT. Below we compare the short wave radiation reaching the vertical  
450 sides of the segment representing the human body computed by BEP-BEM vs those estimated with the more detailed model  
451 TUF-pedestrian.



452

453 Figure A1. Comparison of short wave radiation at the two sides of the vertical segment representing the pedestrian for the  
454 N-S oriented street. Solid line is the WRF, while diamonds are TUF



455

456

457 Figure A2. Same as S1, but for a E-W oriented street









458

459

460 Appendix B. CFD simulations for wind speed variability

461 Data from over 173 microscales CFD simulations of urban airflow are considered over realistic and idealized urban  
 462 configurations, spanning a wide range of building plan area ( $\lambda_p$ ), frontal area ( $\lambda_f$ ), and wall area ( $\lambda_w$ ) densities representative  
 463 of realistic urban neighborhoods in different types of cities. CFD simulations are conducted using 162 large-eddy simulations  
 464 (LES) and 11 Reynolds-averaged Navier–Stokes (RANS) schemes detailed in Table B.1.

Table B.1 Details of CFD microscale simulation cases considered in this study. Simulations are classified based on the configuration (urban form) used. These classifications include **UA** (Uniform height with **A**ligned configuration), **US** (Uniform height with **S**taggered configuration), **VA** (Variable height with **A**ligned configuration), **VS** (Variable height with **S**taggered configuration), **UR** (Uniform height with **R**ealistic configuration), and **VR-WD** (Variable height with **R**ealistic configuration and multiple **W**ind **D**irections considered).

Model	Classification	$H_m$ [m]	$H_{max}$ [m]	$\lambda_p$ range	Count	Source	Example
LES	UA	16	16	[0.0625 - 0.64]	7	Nazarian et al. 2020 Lu et al. 2022	
LES	US	16	16	[0.0625 - 0.64]	7	Nazarian et al. 2020 Lu et al. 2022	
LES	VA	16	20, 24	[0.0625 - 0.64]	42	Lu et al. 2022 Lu et al. 2023	
LES	VS	16	20, 24	[0.0625 - 0.64]	42	Lu et al. 2022 Lu et al. 2023	
LES	UR	16	16	[0.057 - 0.536]	64	Lu et al. 2022	
RANS	VR-WD	14.5-34	variable	[0.190 - 0.680]	11	Sanchez et al. (2017) Santiago et al. (2017) Kracht et al. (2017) Borge et al. (2018) Kracht et al. (2019) Santiago et al. (2020) Sanchez et al. (2021)	

465

466 In the LES simulations, airflow over idealized and realistic urban arrays to determine the model parameters (Nazarian et al.,  
 467 2020; Lu et al., 2022, 2023). Realistic urban layouts are prepared by rasterizing building footprints from an open-source



468 dataset OpenStreetMap using OSM2LES (Lu et al., 2022). 64 realistic urban neighborhoods were obtained assuming  
469 uniform building height (Table B.1) from several major cities such as Sydney and Melbourne (Australia), Barcelona (Spain),  
470 Detroit, Los Angeles, and Chicago (United States). Idealized urban arrays are considered in aligned and staggered  
471 arrangement that follows (Coceal et al., 2007) with varying urban density ( $\lambda_p$  in [0.0625,0.64]) and height variability ( $H_{std}$   
472 =[0m,2.8m,5.6m]). Simulations are conducted in the Parallelized Large-eddy Simulation Model (PALM, version r4554)  
473 (Maronga et al., 2020) following the same setup in (Nazarian et al., 2020), which has validated results against Direct  
474 Numerical Simulation (Coceal et al., 2007) and wind tunnel experiments (Brown et al., 2001). The computational domain is  
475 discretized using the second-order central differences (Piacsek and Williams, 1970) where the horizontal grid spacing is  
476 uniform and the vertical spacing follows the staggered Arakawa C-grid. The minimal storage scheme is employed in the time  
477 integration to solve the filtered prognostic incompressible Boussinesq equations where the pressure perturbation was  
478 calculated in Poisson's equation and was solved by the FFTW scheme (Frigo and Johnson, 1998).

479 The RANS dataset is derived from steady-state CFD-RANS simulations performed with the Realizable k-  $\epsilon$  turbulence  
480 model (STAR-CCM+, Siemens) over realistic urban areas. The size of the computational domains is determined following  
481 the best practice guideline of COST Action 732 (Franke et al., 2010). The horizontal area covers around 1-1.5 km<sup>2</sup> and the  
482 domain top is at around 8H, being H the mean height of buildings. The resolution of the irregular polyhedral mesh used in all  
483 CFD-RANS simulations goes from 0.5 m close to buildings to 6 m out of the built-up area, which results in between 3 and 8  
484 million grid points depending on the complexity of the geometry. Inlet vertical profiles for wind speed, turbulent kinetic  
485 energy (k), and its dissipation ( $\epsilon$ ), are established in neutral atmospheric conditions. The evaluation of the CFD-RANS  
486 simulations was addressed in previous studies summarized in Table B2 and more information is provided in previous  
487 publications.

488